Design of a microNewton Thrust Stand for Low Pressure Characterization of DBD Actuators

J. Soni[1], J. C. Zito[2], and S. Roy[3]
Applied Physics Research Group, University of Florida, Gainesville, Florida, 32608, USA

The design and construction of a torsion balance capable of micronewton resolution is presented. Comparative error analysis of two calibration methods (electrostatic force and logarithmic decrement) is presented, suggesting preference for logarithmic decrement method. Force measurement data from this balance is compared with a commercial precision balance, and found to be in good agreement. Low pressure performance of DBD plasma actuators between a pressure range of 100 to 760 Torr is assessed with the help of this thrust stand. The effect of dielectrics material (Teflon, Kapton) and thickness have been investigated. Experiments suggest that the force first increases upto a certain pressure, after which it drops sharply tending to zero. The amount of force amplification is found to be significant (several-fold) and dependent on the thickness of the dielectric. The power is found to increase with decreasing pressure, resulting in a peak effectiveness a sub-atmospheric pressure.

Nomenclature

A	=	electrode area (m^2)
δ	=	logarithmic decrement (-)
dx	=	displacement (m)
ε	=	permittivity of air (F/m)
F	=	force/thrust (N)
I_Θ	=	Moment of Inertia (Kh-m^2)
k_Θ	=	torsion spring constant (Nm/deg)
l_T	=	thruster distance (m)
l_s	=	sensor distance (m)
L	=	separation gap (m)
Θ	=	angular displacement (deg)
ς	=	damping constant (-)
V	=	voltage (V)
ω_n	=	natural frequency (rad/s)
ω_d	=	damped frequency (rad/s)
x	=	distance (m)

I. Introduction

Dielectric barrier discharge (DBD) actuators have been at the helm of recent research in the field of flow control. They offer unique advantages over rival technologies, such as lack of moving parts, scalability, versatility of design and geometry, and surface compliance. DBD actuators work by virtue of locally injecting momentum into the boundary layer to delay/avoid separation, or alter the shape and characteristics of the flow. DBD plasma have been known and used in the industry for several decades for Ozone generation and sterilization, and consequently the mechanism of the discharge itself is well documented[1,2]. However, in late 1990s, Roth[3-5] popularized a mechanism of generating a directional force by utilizing asymmetrical electrode placement on either side of a dielectric medium. Early results found that indeed these devices induced wall jets along the surface of the dielectric, and extensive work

[1] Graduate Student, Applied Physics Research Group, AIAA Student Member
[2] Graduate Student, Interdisciplinary Microsystems Group, AIAA Student Member
[3] Director Applied Physics Research Group. Associate Professor, University of Florida

has been carried out in the last decade on characterizing the performance of these actuators with respect to geometry[6-8], electrical parameters[9-11], dielectric properties[11-13], surface chemistry[14], and underlying physics[15,16]. Thomas *et al*[17] have written an excellent review of the research done until 2010 on the topic of plasma actuator flow control. However, one main parameter, the operating pressure, has been left missing in these studies and hasn't been studied extensively. As currently understood, the fundamental mechanism of force generation is stipulated to be momentum transfer from ions to neutrals via collisions. Gregory[15] proposed a theoretical analysis based on the collisional model, which suggested a linear decrease in force with neutral number density, and hence with pressure. This model was supplanted with experimental results between a pressure range of 141 to 600 Torr, which demonstrated decent agreement with the linear force reduction hypothesis. However, Abe *et al*[18] found that the force does not decrease monotonically over the entire pressure range, rather increasing first upto a certain pressure, followed by the reducing gradually as predicted by Gregory. The gain in force, however, was not found to be significant, with the peak force (which occurs at around 600 Torr) being only 10% higher than the force at ambient pressure.

The present work was undertaken with the aim of furthering the understanding of plasma actuator performance at low pressures and gaining an insight into the physical mechanism leading to force production. Since plasma generation itself is a strong function of pressure, one can expect a mutual correlation among other quantities with pressure as the unifying parameter. The current study focused on three main parameters: pressure, dielectric thickness, and operating voltage.

II. Experimental Setup

For the purposes of measuring forces below the resolution of the commercial balance, a torsion force balance capable of micronewton resolution was devised. The device is essentially a torsion spring, which undergoes angular deflections under the action of a torque produced by a force. This angular deflection, generated by an unknown force acting at a known distance, can be measured as linear displacement of the balance arm at a known distance from the pivot. The device was first conceived by Charles Coulomb to measure electrostatic forces, which lead to the discovery of the Coulomb Law, and later by Henry Cavendish to measure the gravitational force between two masses. Since the torsion balance is a proportional balance, it needs a-priori calibration before forces can be measured reliably and with known certainty.

Jamison *et al*[19], Zeimer[20], Gamero-Castaño *et al*[21,22], and Koizumi *et al*[23] have all built thrust stands with the same fundamental working principle, albeit with different methods for calibration, damping, and displacement measurement. Table I summarizes the detail and the resolution achieved by each of these.

TABLE I. Review of existing thrust stands with sub-micronewton level resolution

Team	Calibration Source	Damping Mechanism	Displacement Measurement	Resolution	Accuracy
Jamison et al[19]	Orifice Thruster *	Viscous Oil Bath	LVDT	< 1 μN	± 2-16 %
Ziemer[20]	Impact Pendulum @	Damping coil	LVDT	< 1 μN	20%
Gamero-Castaño[21]	Electrostatic #	Electrostatic	Fiber Optic LDS	0.01 μN	
Gamero-Castaño[22]	Electrostatic $	Electrostatic	Fiber Optic LDS	0.03 μN	-
Koizumi et al[23]	Impact Pendulum &	Electromagnetic	LVDT	0.7 μNs	

* orifice thruster was calibrated using DSMC; the lowest thrust measured was 88.8 *nN*.

@ actual steady state thrust measured was 1 μN using a FEEP thruster

lowest thrust measured was 0.11μN using an electrospray source

$ lowest thrust measures was 7.89 μN using a colloid thruster

& only impulse bits generated using diode laser ablation microthruster were measures

A. APRG μNTS : Design Details

The torsion balance presented herein, called the μNewton Thrust Stand (μNTS) henceforth, was conceived as a part of larger experiment to develop a plasma based micro-thruster called the Free Molecular Electro Jet (FMEJ)[24], capable of delivering sub-micronewton level thrust for nanosatellites. The thrust stand aims to resolve forces smaller than 1 micronewton, preferably down to several nanonewtons (~50 nN).

The statics and dynamics of an *undamped* torsion balance are completely characterized by two parameters: the torsion spring constant k_θ, and the Moment of Inertia (MI) of the system I_θ, which govern the natural frequency of the system as,

$$\omega_n = \sqrt{\frac{k_\theta}{I_\theta}} \tag{1}$$

However, for practical concerns, damping is desired to bring the system to a steady state, facilitating quick readings. For such a damped system, the equation of motion is

$$\ddot{\theta} + 2\varsigma\omega_n\dot{\theta} + \omega_n^2\theta = \frac{f(t)l_T}{I_\theta} \tag{2}$$

where $\theta(t)$ is the deflection angle, ς is the damping coefficient, $f(t)$ is the time dependent force, and l_T is the distance from the pivot at which the force forms a torque (moment arm).

For a constant force $f(t)$ = F, Ziemer[20] gives the solution to Eq. 2 as,

$$\theta(t) = \frac{Fl_T}{I_\theta\omega_n^2}\left[1 - e^{-\varsigma\omega_n t} \times \left(\frac{\varsigma}{\sqrt{1-\varsigma^2}}\sin\left(\sqrt{1-\varsigma^2}\,\omega_n t\right) + \sin\left(\sqrt{1-\varsigma^2}\,\omega_n t\right)\right)\right] \tag{3}$$

the steady state solution to which is

$$\theta(t \to \infty) = \frac{F \cdot l_T}{k_\theta} \tag{4}$$

Solving for F,

$$F = \frac{\theta(\infty)\cdot k_\theta}{l_T} \tag{5}$$

Hence, knowing the steady state deflection $\theta(\infty)$, the spring constant k_θ, and the moment arm l_T, the unknown force F can be readily calculated.

Figure 1 shows a 3D rendering of the APRG* μNTS. The two flexure pivots at the vertical ends of the cross-beam form the torsion spring providing the restoring torque. The cross-beam is laterally unsymmetrical to optimize the sensitivity within the space constraints (the entire system must fit inside a vacuum chamber 22" x 20" x 9" in size with enough clearance).

* Applied Physics Research Group

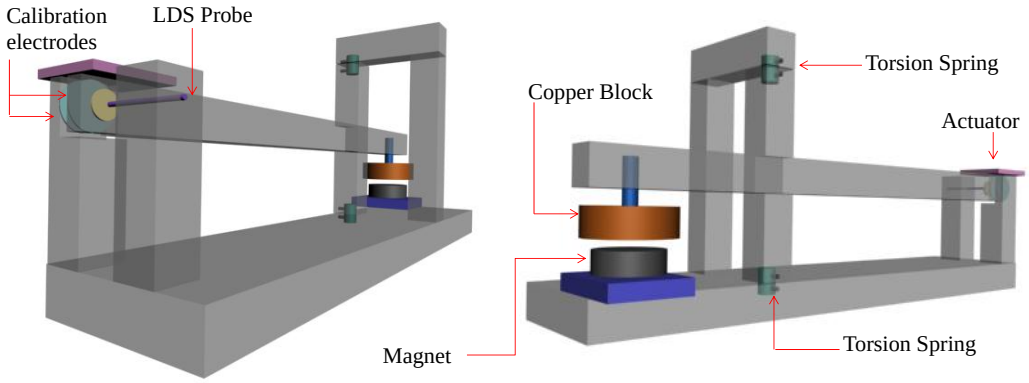

Figure1. Details of the APRG *μ*NTS

The flexure pivots, as a pair, act as the torsion spring. The copper block acts as a counterweight and balances the unsymmetrical beam. A pair of aluminum disc electrodes provides a known force or controlled displacement for calibration. An optical linear displacement sensor (Philtec Model D-63) measures the displacement of the balance arm at a distance to calculate the angular deflection.

For the current design, both the sensor and the calibration electrodes are located at a distance of 28.5 cm from the pivot axis ($l_s = l_T$). The torsion springs, procured from Riverhawk Company, have a rated spring constant of 0.0016 Nm/deg each, with an accuracy of ±10%. In the given configuration, the two torsion spring act in parallel, hence the total spring constant is just a numerical sum giving a mean total spring constant for the system of around 0.0032 Nm/deg. Having these two parameters fixed by design, the resolution of the stand is limited only by the resolution with which the displacements *dx* can be measured, and the accuracy with which the system can be calibrated.

B. APRG μNTS : Damping Mechanism

Damping a dynamical system is of critical importance to counter noise and reduce the time required to reach a stable deflection of the balance arm. In the absence of damping, the balance arm vibrates for a significant duration (Fig. 2(a)), with ambient air providing only minimal damping, apart from structural/thermal dissipation at the torsion springs. To make the system more damped, a magnetic damper was introduced based on eddy current damping. A similar concept was demonstrated for damping structural vibrations of a beam by Sodano *et al*[25]. For the *μ*NTS damper, a cylindrical copper block (2 ½ " dia. x 1" height) of high conductivity was mounted on the balance arm, with a permanent magnet placed under it in close proximity (Fig. 2(b)). As the beam oscillates, the relative motion of the copper block and the magnet produces eddy currents in the block, which generate their own magnetic field counter to the applied magnetic field. The applied and induced magnetic fields interact to produce a force proportional to the relative motion, essentially providing damping. The amount of damping can be controlled by controlling the gap between the copper block and the permanent magnet (Fig. 2c)), and close-to-critical damping can be achieved. Magnetic damping has inherent advantages of being a non-contact damper (as opposed to a viscous damper), and of not requiring a power source (as opposed to an electromagnetic/electrostatic damper).

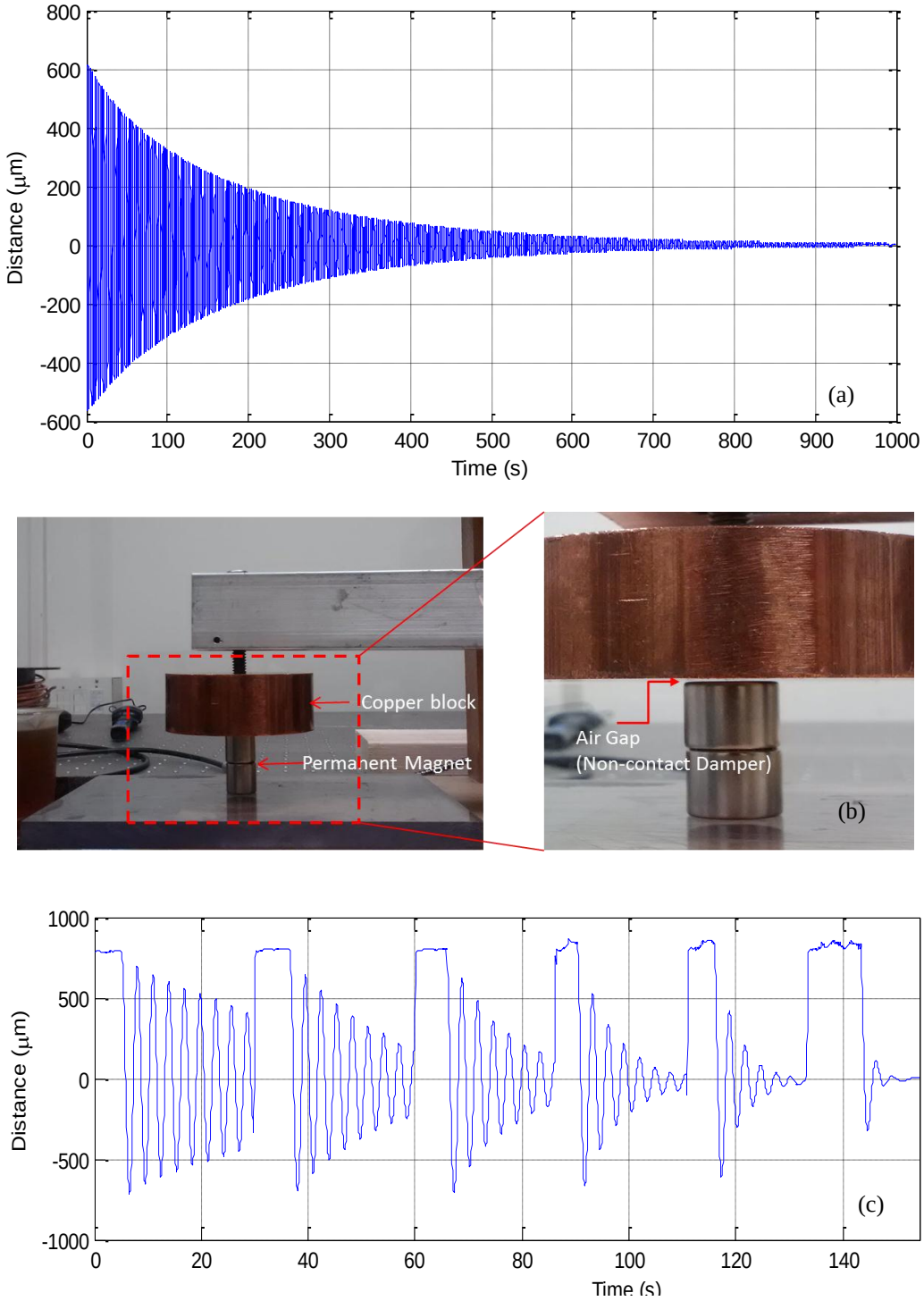

Figure 2. (a) Undamped oscillations, (b) Magnetic damper, (c) damped oscillations with increasing damping

C. APRG μNTS : Calibration

As reported in Table I, several methods of calibration have been reported in literature. Most of these rely on a device which can produce an accurately known force, against which the system is calibrated, with the exception of the Impact pendulum used by Ziemer[20] which relies on applying a known *impulse* instead of a steady-state force to back out the system dynamics. The orifice thruster, used by Jamison *et al*[19], itself is calibrated using DSMC methods, which introduce a certain amount of uncertainty in the exact force that the thruster delivers. The electrostatic force calibration implemented by Gamero-Castaño[21,22] has its own disadvantages. The following error analysis shows that this method inherently introduces multiple sources of error, necessitating a better calibration method.

Consider the electrostatic force calibration. The force between two parallel plate electrodes separated by a distance L and having an area A is given by

$$F = \frac{1}{2}\varepsilon\left(\frac{V}{L}\right)^2 A \tag{6}$$

Combining Eq. 5 and 6, the calibration constant k_θ can be written as,

$$k_\theta = \frac{\varepsilon}{2}\cdot V^2 \cdot \frac{1}{L^2}\cdot A \cdot l^2 \cdot \frac{1}{dx} \tag{7}$$

Applying error propagation analysis to this equation yields the following equation for relative uncertainty in k_θ,

$$\frac{\partial k_\theta}{k_\theta} = \sqrt{\left(\frac{2dV}{V}\right)^2 + \left(\frac{2dL}{L}\right)^2 + \left(\frac{dA}{A}\right)^2 + \left(\frac{2dl}{l}\right)^2 + \left(\frac{dx}{x}\right)^2} \tag{8}$$

As can be seen, there are five sources of error in the above calibration method, some of which can be controlled more precisely than others. The applied voltage *V*, electrode area *A*, and the moment length *l* can be controlled to a fair degree of accuracy. However, the electrode gap *L* (typically 1mm), and the sensor resolution *dx* (50 nm) present the biggest challenge in controlling the spread of the calibration data. Moreover, Analysis suggests that a 10% error in *L* alone leads to nearly 20% error in k_θ. Accounting for errors from the other sources would increase this figure further.

To overcome this limitation, the system was calibrated using three different approaches, and the uncertainty and error sources in these methods were analyzed to choose the optimal method. The first method entailed observing the natural frequency of the undamped system to back out the spring constant using the relation Eq. 1 reformulated as

$$k_\theta = \omega_n^2 \cdot I_\theta \tag{9}$$

The moment of inertia (MI) I_Θ of the system is computed by superposition of the MIs of the component shapes and parallel axis theorem. This gives an estimate of I_Θ = 0.0385 Kgm^2. The natural frequency for the undamped system is observed to be 2.240 rad/s from the Fig 3(a). These values, in conjunction with Eq. (9), give an estimate for k_θ of around 0.0034 N-m/deg, close to the stipulated value of 0.0032 and within the 10% error margin quoted by the manufacturer. Of course, this value of k_θ would only be an approximation of the actual value to a certain error, since the system is not really undamped, as the air around the system provides a small but finite amount of damping. The log-decrement method is used next to calculate exactly how much damping the air provides, and to compute a more precise estimate of k_θ.

The log decrement method[26] backs out the damping ratio of the system based on successive peaks of damped oscillations, which, in conjunction with the observed damped frequency, provides an estimate of the spring constant. For n cycles of a damped oscillation, the logarithmic decrement δ is defined as

$$\delta = \frac{1}{n} \ln \frac{x_0}{x_n} \tag{10}$$

where x_0 and x_n are the amplitudes of the first and n^{th} peaks respectively. The damping ratio ζ is then found using the relation

$$\varsigma = \frac{1}{\sqrt{1 + \left(\frac{2\pi}{\delta} \right)^2}} \tag{11}$$

From the observed damped frequency ω_d and the damping ratio, the natural frequency ω_n can be estimated as

$$\omega_n = \frac{\omega_d}{\sqrt{1 - \varsigma^2}} \tag{12}$$

Finally, the spring constant then can be estimated as

$$k_\theta = \omega_n^2 \cdot I \tag{13}$$

Applying this method to the data extracted from Fig. 2(a), we get an average value of k_θ = 0.003379 N-m/deg based on several values of n, demonstrating that neglecting air damping results in a nominal error of approximately 0.7 %. The damping ratio in this case is found to be around 0.0028, justifying the undamped assumption.

The same analysis is applied to the system when it is damped using the magnetic damper. Since this is the configuration in which the setup will be used for future force measurement, a comprehensive set of calibration reading are taken at varying displacements, to ensure linearity of the spring constant over the desired range of displacement. Increasing displacements are produced using electrostatic force exerted by the parallel electrodes, and the system is set to vibrate by turning off the force. As evident in Fig. 3, calibration values from both the electrostatic force and log decrement method are seen to converge around a value of 0.00345 N-m/deg, with a standard deviation of just over ~ 0.07%. The spread in the data at lower displacements has to do with the fact the LDS signal-to-noise ratio decreases at lower displacement, leading to higher uncertainty in the results. Moreover, a slightly higher value than the nominal 0.0032 Nm/deg is to be expected since the axial and radial loading that the springs are under alters the spring constant slightly. This was further confirmed by a Riverhawk technical representative.

The log-decrement method offers the unique advantage that it is free from any errors in the *source* used to generate the displacement, and depends *only* on the response of the system itself. This greatly reduces the uncertainties associated with calibration process, with the only source of errors being the lower limit on the sensor resolution (which determines the uncertainty in ω_n, and the accuracy with which the Moment of Inertia of the system can be calculated. The uncertainty propagation relation for Eq. 13 would be

$$\frac{\partial k_\theta}{k_\theta} = \sqrt{\left(\frac{2d\omega_n}{\omega_n} \right)^2 + \left(\frac{dI_\theta}{I_\theta} \right)^2} \tag{14}$$

The Moment of Inertia I_θ can be computed to a high degree of certainty using precision a weighing scale and Vernier calipers. A simple uncertainty analysis suggests a good conservative estimate for dI_θ would be 5%. The *relative* uncertainty estimate for ω_n is not so straightforward since it depends on the way the errors in x_0 and x_n propagate thru Eq. 10, 11. and 12, resulting in an estimate which depends on the actual values of δ, ζ, and ω_n. Reasonable estimations based on typical values of ζ (~0.14) suggest a 10% spread in ω_n. These error estimates gives an error estimate of 20.6% for k_θ. Figure 4 suggests the statistical scatter in k_θ is also of the same order; hence the data obtained using the μNTS is quoted with the statistical error as error bars instead. Zito *et al*[27] have used the μNTS setup for thrust measurement of microactuators, thus validating its resolution.

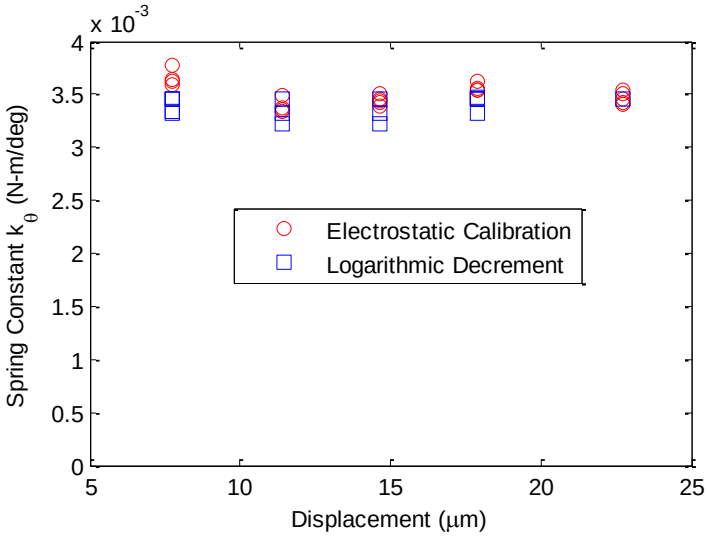

Figure 3. μNTS Calibration : Comparison between electrostatic force calibration and log decrement method

D. Power supply setup

DBD actuators typically require an alternating potential of several kilovolts at kilohertz frequencies across the electrodes to initiate a discharge. To achieve this, a signal of desired shape and frequency (Sine in this case) is generated using a Tektronix AFG3022B function generator. This signal is stepped up using a Crown CDi4000 audio amplifier for a gain of around 24. Further amplification by a gain of 220 takes place through a high-voltage transformer (Corona Magnetics, Inc. CMI 5523). A current probe (Pearson Electronic 2100) and a high voltage probe (Tektronix P6015A) capture the current and voltage data through a digitizing oscilloscope (Tektronix DPO2014). Figure 4 schematically illustrates this setup.

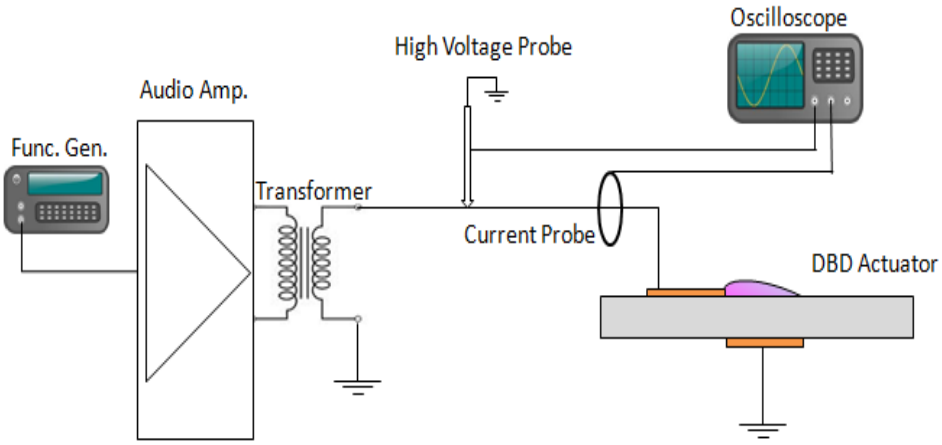

Figure 4. Electrical setup for powering the Actuators

To check how the μNTS compares against a commercial balance, a test actuator was designed and tested on both the μNTS, and a commercial precision balance (Ohaus Adventurer Pro™ AC313C, 1 mg resolution). The actuator consisted of 1.5mm thick acrylic with 5mm powered electrode and a 20mm ground. The upstream edge of the powered electrode was covered to prevent reverse discharge, and the ground electrode was covered with several layers of electrical tape. The actuator mounted on the commercial precision balance was 95mm long (to produce enough force to assure a high signal-to-noise ratio), whereas the actuator mounted on the μNTS was 20mm in length due to space and displacement constraints on the μNTS. The force data from thr μNTS, shown in Fig. 5, suggests decent agreement with between the two balances. We see that direct force measurement from the μNTS start diverging at higher voltage (above 15 kVpp). This might have to do the different downstream plate lengths of the two actuators, being shorter in case of the 20mm actuator. Durcher and Roy[28] have demonstrated that indeed a shorter downstream plate length leads to a higher force (by upto 20%) due to decreased drag loss along the plate surface.

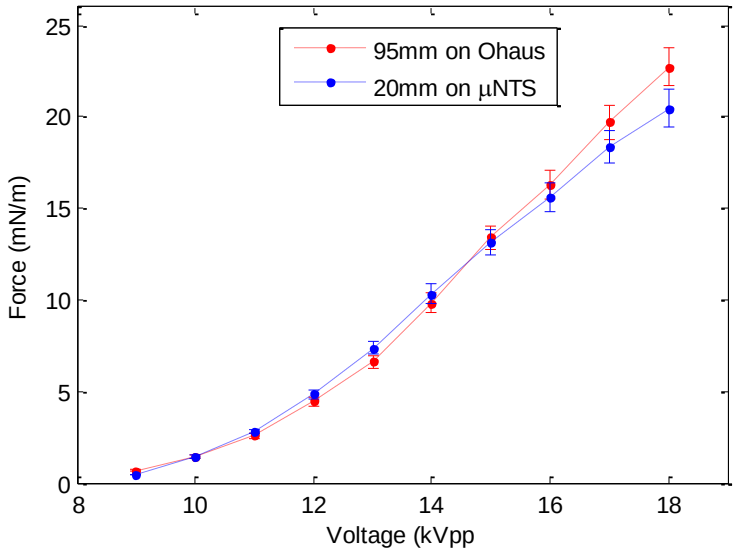

Figure 5. Comparison of force measurement from commercial precision balance and μNTS

III. DBD Actuator Performance at Low Pressure

Most of the performance characterization studies on DBD actuators focus on operation at ambient pressure. However, potential areas of application of these actuators often involve non-ambient pressure regimes (airfoil wings, planetary probes). Gregory[15] has proposed a theoretical model of the force production mechanism in plasma actuators, which predicts a linear reduction in force with pressure. This was augmented with experimental data between a pressure range of 584 Torr down to 141 Torr. Abe *et al*[18] conducted experimental investigations in a pressure range of 760 Torr down to 188 Torr, and found the force to increase slightly before resuming the linear reducing trend reported by Gregory. Their work also demonstrated the dependence of the force on the composition of the working fluid (air, CO_2, N_2), and the material and the geometry of the electrodes (stainless steel v. copper, metal tape v. wire mesh). However, the peak force, which occurred at a pressure of around 600 Torr, was only marginally (10%) higher than the force at ambient pressures, suggesting only a minor gain.

In the present work, the actuators tested are 4cm in length, with 5mm wide powered and ground electrodes. The upstream edge of the powered electrode is covered with Kapton tape to prevent reverse discharge, and the ground electrode is covered with either several layers of insulation tape. The electrodes themselves made of 40 micron thick copper tape. Figure 6 illustrates the actuator configuration, and Table II provides details of the dielectrics tested and the parameters studies.

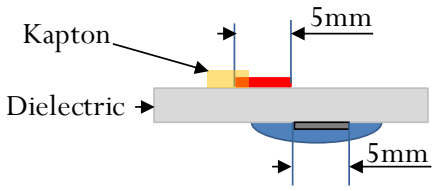

Figure 6. Actuator electrode configuration

TABLE II. Details of the actuators tested on the *μ*NTS

Material	Thickness (mil, mm)	Voltage (kVpp)	Frequency
Kapton	2 mil	6	14 kHz
Teflon	5 mil 10 mil	6	

IV. Results

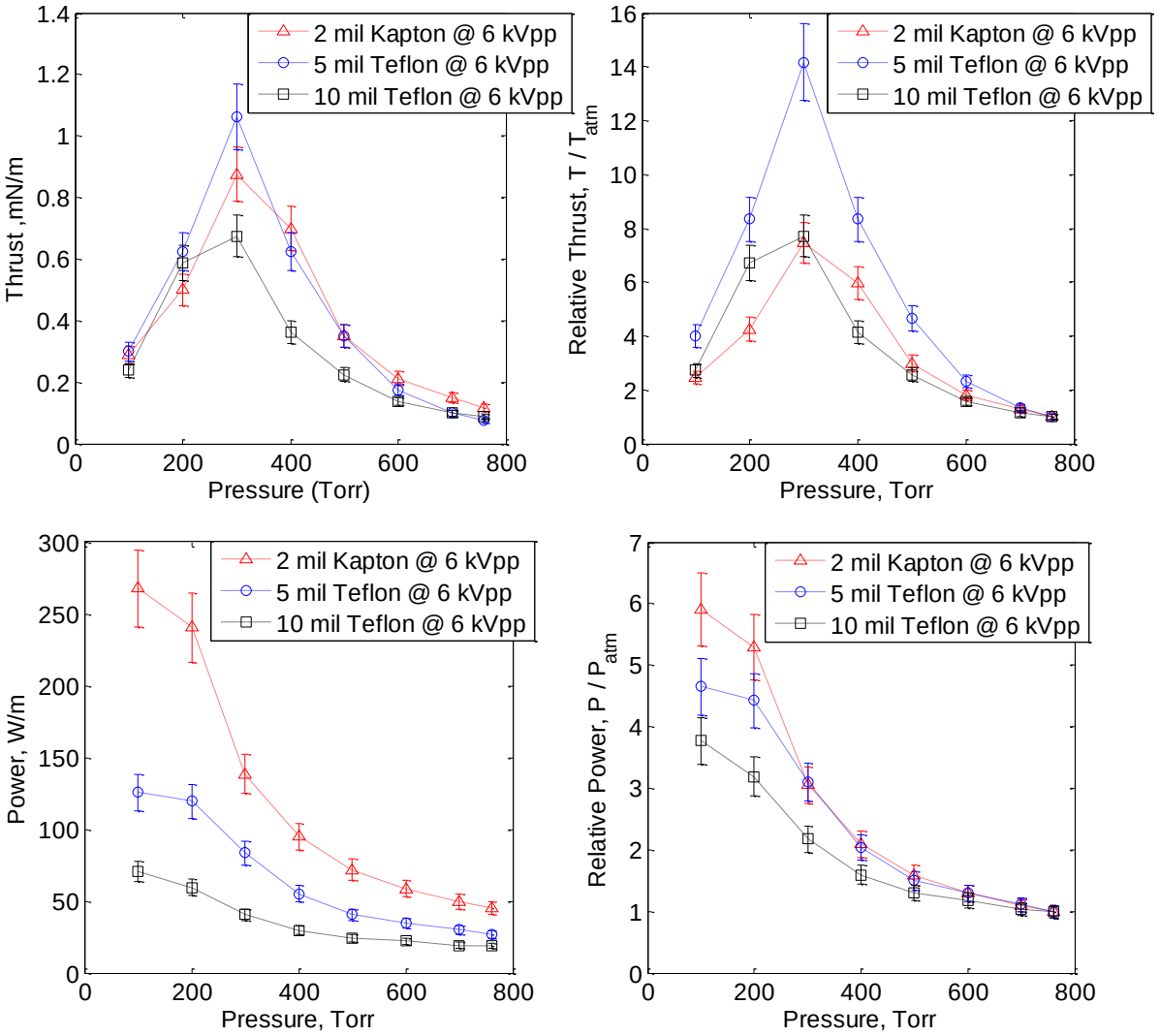

Figure 7. Force and Power trends *Absolute (top), Normalized by ambient values (bottom)*

Figure 7 shows the force versus pressure and power versus pressure trends for the actuators. Both absolute and normalized values are shown to give an idea of % change in the parameters. The normalization is done with respect to the corresponding values at ambient pressure. It is seen that in all the cases, the force first increases up t a certain pressure, before dropping down and tending to zero. The pressure at which the force reaches a maximum is seen to be more or less the same at around 300 Torr. The 2 mil Kapton and 5 mil Teflon produce about the same force until this inversion point, beyond which the Teflon actuator is seen to produce a higher force. The amplification in force at low pressures is seen to be several-fold in all cases. However, in case of Teflon, the thinner dielectric (5 mil) is seen to achieve much more amplification (15-fold) compared to the thicker one (10 mil, 8-fold). This hints towards a dependence of force amplification on dielectric thickness, which needs experimental verification.

The power consumption is seen to increase as the pressure goes down, which is expected from the visual evidence that the plasma extent keeps growing as the pressure goes down until it covers the entire width of the ground electrode. The increase in power consumption is seen to be several-fold, being higher for thinner dielectrics than thicker ones for the same dielectric (Teflon). However for different dielectrics (2 mil Kapton and 5 mil Teflon), the increase in power is almost identical until the pressure corresponding to peak force (300 Torr), after which power consumption in 2 mil Kapton is seen to be increasing more than 5 mil Teflon.

The inflexion point in the force trend and the absence of it in the power trend suggests that the actuator effectiveness (force produced per unit power consumed) might also peak at a sub-atmospheric pressure. Figure 8 demonstrates that this is indeed the case. It is seen that the 10 mil Teflon actuator has the highest effectiveness of the three, followed by 5 mil Teflon and 2 mil Kapton respectively. This is interesting since the force produced is the smallest for10 mil Teflon. However, what renders it superior in effectiveness is the fact that the power consumption is the least for 10 mil Teflon, thus leading to a high effectiveness. The increase in effectiveness is seen to be more in 5 mil Teflon than in 10 mil Teflon, and least in 2 mil Kapton. This suggests that the Kapton actuator might be operating in the thrust saturation regime based on the minimal electric field it is under. Thrust saturation for Kapton at 72 MV/m has been demonstrated by Durscher and Roy[12]. The electric field across the current Kapton actuator is approximately 60% higher than this value, providing reasonable grounds to suspect the actuator is operating in or around the thrust saturation region, leading to sub-optimal thrust and effectiveness figures.

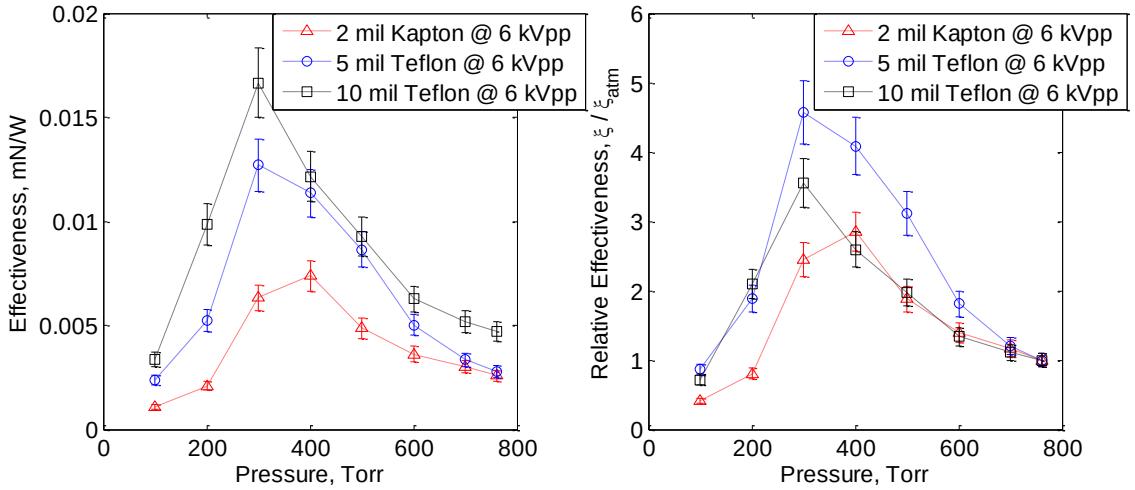

Figure 8. Actuator Effectiveness *Absolute (left), Normalized by ambient values (right)*

V. Conclusion

Low pressure performance of DBD actuators using a custom torsional force balance suggests that the force first increases upto a pressure of approximately 300 Torr, and then drops sharply as the pressure is further reduced to down 100 Torr. The increase in force is found to be significant (several-fold) for the dielectrics and the thicknesses tested. The power is seen to increase continually as the pressure goes down, and this leads to a peak effectiveness at a sub-atmospheric pressure. The increase in effectiveness is also seen to undergo a several-fold increase, and the pressure at which this occurs is seen to coincide with the peak force pressure. These results need further experimental verification to obtain an insight into the physics leadings to the observed results.

VI. References

[1]Kogelschatz, U., "Dielectric-barrier Discharges: Their History, Discharge Physics, and Industrial Applications", *Plasma Chemistry and Plasma Processing*, Vol. 23, March 2003.

[2]Kogelschatz, U, "Filamentary, Patterned, and Diffuse Barrier Discharges", *IEEE Transactions on Plasma Science.* Vol. 30, August 2002.

[3]Roth, J. R., Sherman, D. M., and Wilkinson, S. P., "Boundary Layer Flow Control with a One Atmosphere Uniform Glow Discharge Surface Plasma", *36th Aerospace Sciences Meeting & Exhibit*, Reno, NV, 1998.

[4] Roth, J. R., "Electrohydrodynamically Induced Airflow in a One Atmosphere Uniform Glow Discharge Surface Plasma", *IEEE International Conference on Plasma Science*, Piscataway, NJ, 1998.

[5]Roth, J. R., Sherman, D. M., and Wilkinson, S. P. "Electrohydrodynamic Flow Control with a Glow-Discharge Surface Plasma", *AIAA Journal*, Vol. 38. 2000, pp. 1166–1172.

[6]Hoskinson, R., Hershkowitz, N., "Differences between dielectric barrier discharge plasma actuators with cylindrical and rectangular exposed electrodes", *J. Phys. D: Appl. Phys.*, Vol. 43, 065205, 2010.

[7]Wang, C.-C., Durscher, R., Roy, S., "Three-dimensional effects of curved plasma actuators in quiescent air", *J. Appl. Phys.*, Vol. 109, 083305, 2011.

[8]Wang, C.-C., Roy, S. "Geometry Effects of Dielectric Barrier Discharge on a Flat Surface", *49th AIAA Aerospace Sciences Meeting*, Orlando, FL, 2011. AIAA-2011-732.

[9]J.C. Zito, D.P. Arnold, R.J. Durscher, S. Roy,. "Investigation of Impedance Characteristics and Power Delivery for Dielectric Barrier Discharge Plasma Actuators", *48th AIAA Aerospace Sciences Meeting*, Orlando, FL, 2010, AIAA-2010-964.

[10]Zhao, P., Roy, S., "Study of Spectrum Analysis and Signal Biasing for Dielectric Barrier Discharge Actuator", *50th AIAA Aerospace Sciences Meeting*, Nashville, TN, 2012, AIAA-2012-0408.

[11]Thomas, F. O., Corke, T. C., Iqbal, M., Kozlov, A., Schatzman, D., "Optimization of Dielectric Barrier Discharge Plasma Actuators for Active Aerodynamic Flow Control", *AIAA Journal*, Vol. 47, Sept 2009.

[12]Durscher, R., Roy, S., "Aerogel and ferroelectric dielectric materials for plasma actuators", *J. Phys. D: Appl. Phys.*, 2012, Vol. 45. 012001.

[13]Durscher, R. J., Roy, S., "On Multi-Barrier Plasma Actuators", *49th AIAA Aerospace Sciences Meeting*, Orlando, FL, 2011, AIAA-2010-958.

[14]Fine, N. E., Brickner, S. J., "Plasma Catalysis for Enhanced-Thrust Single Dielectric Barrier Discharge Plasma Actuators", Technical Notes, *AIAA Journal*, Vol. 48, No. 12, December 2010

[15]Gregory, J. W., Enloe, C. L., Font, G. I., McLaughlin, T. E., "Force Production Mechanisms of a Dielectric-Barrier Discharge Plasma Actuator", *45th AIAA Aerospace Sciences Meeting and Exhibit*, Reno, Nevada, January 2007.

[16]Mestiri, R., Hadaji, R., Ben Nasrallah, S., "An experimental study of a plasma actuator in absence of free airflow: Ionic wind velocity profile", *Physics of Plasmas*, Vol. 17. 2010, 083503.

[17]Corke, T. C., Enloe. L. C., Wilkinson, S. P., "Dielectric Barrier Discharge Plasma Actuators for Flow Control", *Annu. Rev. Fluid Mech.*, Vol. 45., 505-29, 2010

[18]Abe, T., Takizawa, Y., Sato, S., "Experimental Study for Momentum Transfer in a Dielectric Barrier Discharge Plasma Actuator", *AIAA Journal*, Vol. 46, No. 9, 2008.

[19]Jamison, A., Ketsdever, A., Muntz, E.P., "Accurate Measurement of Nano-Newton Thrust for Micropropulsion System Characterization", *International Electric Propulsion Conference, 2001*, IEPC-01-236.

[20]Ziemer, J. K., "Performance Measurements Using a Sub-Micronewton Resolution Thrust Stand", *International Electric Propulsion Conference*, Pasadena, CA, 2001, IEPC-01-238

[21]Gamero-Castaño, M., Hruby, V., Manuel, M.-S., "A Torsional Balance that Resolves Sub-micro-Newton Forces", *27th International Electric Propulsion Conference*, Pasadena, CA, 2001. IEPC-01-235.

[22]Gamero-Castaño, M., "A torsional balance for the characterization of microNewton thrusters", *R. Sci. Inst.*, Vol. 74., No. 10, 2003.

[23]Koizumi, H., Komurasaki, K., Arakawa, Y., "Development of thrust stand for low impulse measurement from microthrusters", *R. Sci. Inst.*, Vol. 75, No. 10, 2004.

[24]Roy, S., "Method and Apparatus for Small Satellite Propulsion". 61/304,915, WO/2011/103194A2 UF Patent Application, August 25, 2011.

[25]Sodano, H. A., Bae, J-S., Inman, D. J., Belvin, W. K., "Improved Concept and Model of Eddy Current Damper", *Transactions of the ASME*, Vol. 128, June 2006.

[26]Zito, J.C., Arnold, D.P., Houba, T., Soni, J., Durscher, R., and Roy, S., "Microscale dielectric barrier discharge plasma actuators: performance characterization and numerical comparison", 43rd AIAA Plasmadynamics and Lasers Conf., AIAA Paper 2012-3091, New Orleans, LA, AIAA, 06/2012

[27]Zito, J. C., Durcher, R. J., Soni, J., Roy, S., Arnold, D. P., "Flow and force inducement using micron size dielectric barrier discharge", *Applied Physics Letters*, Vol. 100, 2012, 193502.

[28]Durscher, R. J., Roy, S., "Evaluation of thrust measurement techniques for dielectric barrier discharge actuators", *Exp. Fluids*, Vol. 53. 2012, 1165–1176.